



**HAL**  
open science

# In situ synthesis and improved photoelectric performances of a $\text{Sb}_2\text{Se}_3/\beta\text{-In}_2\text{Se}_3$ heterojunction composite with potential photocatalytic activity for methyl orange degradation

D. Ren, O. Merdrignac-Conanec, V. Dorcet, M. Cathelinaud, Z. Zheng, Hongli Ma, Xianghua Zhang

## ► To cite this version:

D. Ren, O. Merdrignac-Conanec, V. Dorcet, M. Cathelinaud, Z. Zheng, et al.. In situ synthesis and improved photoelectric performances of a  $\text{Sb}_2\text{Se}_3/\beta\text{-In}_2\text{Se}_3$  heterojunction composite with potential photocatalytic activity for methyl orange degradation. *Ceramics International*, 2020, 46 (16), pp.25503-25511. 10.1016/j.ceramint.2020.07.021 . hal-02960339

**HAL Id: hal-02960339**

**<https://hal.science/hal-02960339>**

Submitted on 26 Sep 2022

**HAL** is a multi-disciplinary open access archive for the deposit and dissemination of scientific research documents, whether they are published or not. The documents may come from teaching and research institutions in France or abroad, or from public or private research centers.

L'archive ouverte pluridisciplinaire **HAL**, est destinée au dépôt et à la diffusion de documents scientifiques de niveau recherche, publiés ou non, émanant des établissements d'enseignement et de recherche français ou étrangers, des laboratoires publics ou privés.



Distributed under a Creative Commons Attribution - NonCommercial 4.0 International License

**In situ synthesis and improved photoelectric performances of a  
Sb<sub>2</sub>Se<sub>3</sub>/β-In<sub>2</sub>Se<sub>3</sub> heterojunction composite with potential  
photocatalytic activity for methyl orange degradation**

Donglou Ren<sup>a</sup>, Odile Merdrignac-Conanec<sup>a</sup>, Vincent Dorcet<sup>b</sup>, Michel Cathelinaud<sup>a</sup>,

Zhuanghao Zheng<sup>c</sup>, Hongli Ma<sup>a</sup>, Xianghua Zhang<sup>a,\*</sup>

<sup>a</sup>ISCR (Institut des Sciences Chimiques de Rennes)-CNRS, UMR 6226, Univ.

Rennes, F-35000, Rennes, France

<sup>b</sup>Univ Rennes, CNRS, ISCR-UMR 6226, ScanMAT-UMS 2001, F-35000, Rennes,

France

<sup>c</sup>Shenzhen Key Laboratory of Advanced Thin Films and Applications, College of

Physics and Optoelectronic Engineering, Shenzhen University, Shenzhen, 518060,

China

\*Corresponding author: E-mail: [xzhang@univ-rennes1.fr](mailto:xzhang@univ-rennes1.fr)

Tel.: (+33) 02 23 23 69 37

## Abstract

A series of  $\text{Sb}_2\text{Se}_3/\beta\text{-In}_2\text{Se}_3$  heterojunction composites with different contents of  $\beta\text{-In}_2\text{Se}_3$  were successfully synthesized via an in-situ melt-quenching method. The relationship between structure and photoelectric performances was systematically investigated by X-ray diffraction, scanning electron microscopy, transmission electron microscopy, energy-dispersive spectrometry, UV-Vis optical absorption, and photoelectrochemical measurement. The direct band energy of the composites was in the range of 1.15-1.18 eV, implying strong visible light harvesting ability. Meanwhile, the number of heterojunctions and the connectivity of  $\beta\text{-In}_2\text{Se}_3$  crystals could be adjusted by changing the content of  $\beta\text{-In}_2\text{Se}_3$ . As a result, the optimized composites ( $\text{Sb}_2\text{Se}_3\text{-10}\% \beta\text{-In}_2\text{Se}_3$ ) exhibited remarkable photocurrent density that was about 283 times higher than that of pure  $\text{Sb}_2\text{Se}_3$ . Moreover, the response and recovery times were faster than that of previous reported  $\text{Sb}_2\text{Se}_3$ . The interface charge separation and transport mechanism for the improved photoelectric performances was proposed based on the experimental results. Thanks to the remarkable photocurrent density, a potential application was also evaluated by photocatalytic degradation of MO (Methyl Orange) solution. After 180 min of illumination, 76% of MO dye could be decomposed. This work will provide the direct guidance for constructing  $\text{Sb}_2\text{Se}_3/\beta\text{-In}_2\text{Se}_3$  heterojunction devices for harvesting solar energy.

**Keywords:**  $\text{Sb}_2\text{Se}_3/\beta\text{-In}_2\text{Se}_3$  heterojunctions, Photoelectric performances, MO degradation, Photocatalysis, Band structure

## 1. Introduction

The energy crisis and environmental pollution are two serious worldwide issues. During the past decades, intensive research on inorganic semiconductor heterojunctions has promoted the development of electronic device, particularly optoelectronic devices. Composites consisted of heterojunctions stand out in this realm due to the influence of interface electric field resulting from the junction of two different materials, **with potential applications in solar cells**, sensors and for heterogeneous photocatalysis [1-3]. Commons issues with these materials are the cost/scarcity and the toxicity. As an important metal chalcogenide semiconductor, orthorhombic antimony selenide ( $\text{Sb}_2\text{Se}_3$ ) has many outstanding features such as a narrow direct band gap (1.17 eV) [4], a high absorption coefficient ( $> 10^5 \text{ cm}^{-1}$ ) [5] and a high Seebeck coefficient ( $1,800 \mu\text{VK}^{-1}$ ) [6]. Besides, it is also a simple, non-toxic, highly earth-abundant, low-cost and intrinsic p-type semiconductor material [7]. **It thus has emerged as a qualified candidate for different applications such** as solar cells [8,9], photodetectors [6], photoelectrochemical cells [10] and thermoelectric devices [11]. **Despite its huge potential, this material has intrinsically low electrical conductivity ( $10^{-8} \text{ S}\cdot\text{cm}^{-1}$ ) [12] and numerous studies have been made in order to address this issue.** For instance, doping with low-valence metal cations was reported [13,14] and the photocurrent density and responsivity were approximately 14 and 19 times as compared to undoped  $\text{Sb}_2\text{Se}_3$ , respectively. Hybridization of  $\text{Sb}_2\text{Se}_3$  with a high electrical conductivity semiconductor, such as  $\text{Sb}_2\text{Se}_3/\text{Ag}_2\text{Se}$  and  $\text{Sb}_2\text{Se}_3/\text{Cu}_2\text{GeSe}_3$ , to create heterojunction is another strategy for enhancing charge separation and transfer [6,15]. Compared with pure  $\text{Sb}_2\text{Se}_3$ , the

photocurrent densities were about 7 and 100 times for these two heterojunctions, respectively. The enhanced photoelectric performance is attributed to the interface electric field that can efficiently facilitate the separation and transport of the charge carriers. However, the direct band gap is 3 and 0.78 eV for Ag<sub>2</sub>Se and Cu<sub>2</sub>GeSe<sub>3</sub>, respectively, which is far from the optimum value required for efficient visible light absorption [15,16]. Hence, it is essential to search an alternative semiconductor material to construct Sb<sub>2</sub>Se<sub>3</sub>-based heterojunction for further enhancing the photoelectric performances under visible illumination.

As an important semiconductor, indium selenide (In<sub>2</sub>Se<sub>3</sub>), has renewed interest in energy conversion and storage due to its narrow-gap, intrinsic n-type semiconductor and efficient visible-light absorption [17-22]. It is commonly held that In<sub>2</sub>Se<sub>3</sub> is a complicated material, with several possible phases ( $\alpha$ ,  $\beta$ ,  $\gamma$ ,  $\delta$  and  $\kappa$  phases) according to the temperature and material synthesis conditions [23-26]. **Among them, high temperature phase  $\beta$ -In<sub>2</sub>Se<sub>3</sub> is promising for photovoltaic application due to a narrow direct band gap of 1.31 eV** [27]. It belongs to the  $R\bar{3}m$  space group and the lattice parameters are  $a = b = 4.00 \text{ \AA}$  and  $c = 28.33 \text{ \AA}$  [28]. It is composed of quintuple (Se-In-Se-In-Se) layers that are bonded to each other through weak van der Waals interactions along the [001] plan [29]. Despite its huge potential, it is rarely reported/studied owing to its metastability [30]. According to a previous work [31],  $\beta$ -In<sub>2</sub>Se<sub>3</sub> can be stabilized at room temperature by doping with Sb, achieving a narrow band gap of 1.34 eV and a good conductivity of  $2 \times 10^{-2} \text{ S}\cdot\text{cm}^{-1}$ . The band gap value is very close to the optimum value required for single junction photovoltaic solar cells.

Thus, it is interesting to develop hybrid p-n heterojunctions between  $\text{Sb}_2\text{Se}_3$  and  $\beta\text{-In}_2\text{Se}_3$ . This strategy not only can lead to stable  $\beta\text{-In}_2\text{Se}_3$  (Sb-doped) but also synthesize composites with excellent photoelectric performances under visible illumination.

Herein, in this work, a series of  $\text{Sb}_2\text{Se}_3/\beta\text{-In}_2\text{Se}_3$  heterojunction composites with different contents of  $\beta\text{-In}_2\text{Se}_3$  were successfully synthesized by an in-situ melt-quenching method (Fig. 1). The morphologies, composition, optical properties and photo-electro-chemical (PEC) performances of the prepared samples were deeply investigated. Compared with pure  $\text{Sb}_2\text{Se}_3$ , the optimized  $\text{Sb}_2\text{Se}_3/\beta\text{-In}_2\text{Se}_3$  heterojunction composites possessed remarkable photoelectric performances. Moreover, the interface charge separation and transport mechanism was proposed based on the experimental results. Ultimately, a potential application was also evaluated by photocatalytic degradation of MO solution. We believe this work will provide direct guidance for constructing  $\text{Sb}_2\text{Se}_3/\beta\text{-In}_2\text{Se}_3$  heterojunction devices for harvesting solar energy.

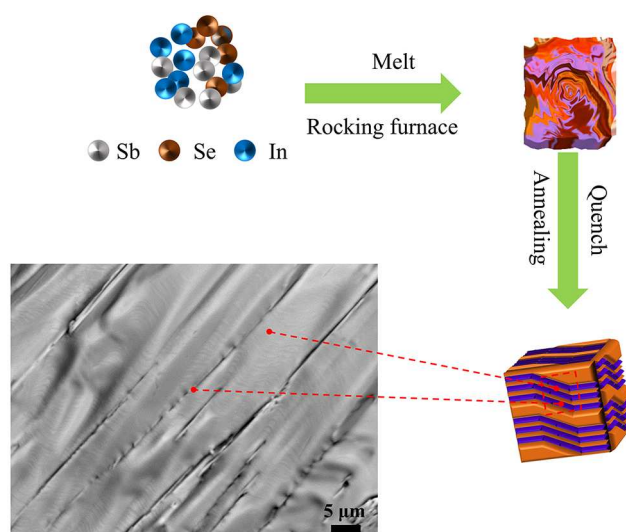


**Fig. 1.** Schematic illustration of  $\text{Sb}_2\text{Se}_3/\beta\text{-In}_2\text{Se}_3$  heterojunction composite.

## 2. Experimental section

## 2.1. Sample preparation

The samples were prepared in bulk form by the melt-quenching method in sealed silica tube at high temperature. The elemental materials Indium (In), Selenium (Se) and Antimony (Sb) of 99.999 % purity were used as raw materials, which were first weighted (12 g mixture for each sample) according to the composition and then loaded into a quartz ampoule of 10 mm in diameter and 15 cm in length in a glovebox under argon. Afterwards, the silica tube was pumped to a vacuum of about  $10^{-5}$  mbar and flame-sealed. The tube containing raw materials was placed in a rocking furnace and heated to 700 °C with 1.2 °C/min ramp. In order to ensure proper mixing and reaction, it was continuously rocked for 8 h at 700 °C, after which the tube was cooled at a rate of 1 °C/min to 650°C. The tube was subsequently quenched in water to ambient temperature and annealed at 350 °C for 3 h for reducing the mechanical stress formed during the quenching process. The as-prepared samples were then removed from the quartz ampoule, cut and polished into discs of 2 mm in thickness for subsequent characterization. According to the composition, the samples are denoted as SI-1.2%, SI-2.5%, SI-5%, SI-7.5% and SI-10%, the number representing the  $\beta$ -In<sub>2</sub>Se<sub>3</sub> molar fraction in the samples.

## 2.2. Characterization

The crystalline phases of the as-prepared samples were characterized by X-ray diffraction (XRD, Bruker AXS D8 Advance X-ray diffractometer) with Cu K $\alpha$  source ( $\lambda = 0.15406$  nm) at room temperature, while the accelerating voltage and the emission current were 40 kV and 40 mA, respectively. The surface morphology of these

specimens was observed by a thermal field emission scanning electron microscope (SEM, JEOL JSM-7100F) at an accelerating voltage of 20 kV. Elemental compositions were determined by energy dispersive X-ray spectroscopy (EDS). **Transmission electron microscopy (TEM), high-resolution transmission electron microscopy (HRTEM) and selected area electron diffraction (SAED) images were obtained from a transmission electron microscope (JEOL 2100) operating at 200 kV.** The electrical conductivity was characterized in the dark using the 4-probe method. Diffuse reflectance spectroscopy (DRS, UV-2550, Shimadzu, Japan) equipped with an integrating sphere was used to determine the optical absorption spectra and the band gap of as-prepared samples in the wavelength range of 300-2500 nm with a reflectance standard of fine BaSO<sub>4</sub> powders. The photo-electro-chemical (PEC) performances were measured using a traditional three-electrode configuration in a LiClO<sub>4</sub> electrolyte (0.5 M). The as-prepared samples acted as the working electrode, Pt wire as the counter electrode, and saturated Ag/AgCl electrode as the reference electrode. A white light tungsten halogen lamp was used as light source during measurement process. More details can be found in our previous work [32].

### 2.3. Photocatalytic activity measurement for MO dye

The potential application of the SI-10% sample, with the highest photocurrent density, was evaluated by methyl orange (MO) degradation experiments under white light illumination, provided by a white LED (100 W). The suspension containing 0.8 g of SI-10% sample as the photocatalyst in the MO solution (80 mL, 10 mg/L) was placed at a distance of approximately 10 cm from the light. Before illumination, the suspension

was stirred for 1 h in the dark until reaching the adsorption-desorption equilibrium. Then, the suspension was exposed to light illumination under constant stirring. At a certain period of time, 2 mL of suspension was collected and filtered by a 0.2  $\mu\text{m}$  filter to remove the photocatalyst. The absorption spectrum of the resulting supernatant was measured by a UV-vis spectrophotometer (UV2550, Shimadzu, Japan) in the wavelength range from 300 to 600 nm with deionized water as a reference sample. **The Brunauer-Emmett-Teller (BET) method was used for the determination of the specific surface of the powders by measuring nitrogen adsorption isotherms at -196 °C on a Gemini VII volumetric adsorption analyzer from Micromeritics. Prior to measurements, the samples were outgassed during one night at 100 °C in a VacPrep 061 degas system (from Micromeritics).**

### **3. Results and discussion**

#### 3.1. Characterization of phase purity and formation mechanism of $\beta\text{-In}_2\text{Se}_3$

The crystallographic and chemical purities of the as-prepared samples were characterized by the powder X-ray diffraction (XRD) analysis. Fig. 2 presents the XRD of samples prepared by in-situ melt-quenching approach with different  $\beta\text{-In}_2\text{Se}_3$  contents. Except for pure  $\text{Sb}_2\text{Se}_3$ , the XRD pattern of all other samples shows diffraction peaks of  $\text{Sb}_2\text{Se}_3$  and  $\beta\text{-In}_2\text{Se}_3$ , corresponding to JCPDS 15-0861 and JCPDS 35-1056 **without any trace of impurity phases**. The intensity of diffraction peaks of  $\beta\text{-In}_2\text{Se}_3$  increases with increasing contents of  $\beta\text{-In}_2\text{Se}_3$ .

Meanwhile, it can be seen that the (006) XRD peak of  $\beta\text{-In}_2\text{Se}_3$  has an obvious shift towards the lower angle (Fig. 2b). The shift may be explained as follows. 1/3 of

In cation sites are vacant in  $\text{In}_2\text{Se}_3$  along the  $ab$ -direction [33,34] and  $\text{Sb}^{3+}$  (0.74 Å) [35] can occupy these vacant sites due to a small ionic radius. Similar phenomenon was already reported by other authors in  $\text{Zn}^{2+}$  (0.74 Å) [36] doped  $\alpha$ - $\text{In}_2\text{Se}_3$  [37] as well as during the formation of  $\text{CuInSe}_2$  [38]. Consequently, the high temperature phase,  $\beta$ - $\text{In}_2\text{Se}_3$  can exist at room temperature due to Sb-doping, in agreement with previous report [31]. There is no detected shift for the (120) XRD peak of  $\text{Sb}_2\text{Se}_3$  in Fig. 2c, which is also in agreement with the fact that cationic doping of  $\text{Sb}_2\text{Se}_3$  is difficult, leading often to phase separation as it was the case of Sn doped  $\text{Sb}_2\text{Se}_3$  for example [13].

Based on earlier reports [18,31],  $\text{Sb}_2\text{Se}_3$ - $\text{In}_2\text{Se}_3$  system is a pseudo-binary system without any defined compound. The formation mechanism of the high temperature  $\beta$ - $\text{In}_2\text{Se}_3$  phase was as follows:  $\alpha$ - $\text{In}_2\text{Se}_3$  was first formed and then transformed into  $\beta$ - $\text{In}_2\text{Se}_3$  when the temperature was raised to 350°C [31]. When the temperature was raised to approximately 650 °C,  $\beta$ - $\text{In}_2\text{Se}_3$  was transformed into  $\gamma$ - $\text{In}_2\text{Se}_3$  [27,39]. According to the phase diagram [31], **the material is liquid**, when the temperature is higher than 700 °C, in form of mixtures in our work. The  $\gamma$ - $\text{In}_2\text{Se}_3$  was gradually transformed into  $\beta$ - $\text{In}_2\text{Se}_3$  during cooling process. Only  $\beta$ - $\text{In}_2\text{Se}_3$  and  $\text{Sb}_2\text{Se}_3$  existed in the final products after the quick quenching from 650 °C to room temperature, resulting from the Sb doping. Melt method is beneficial to liquid mass transfer, leading to homogeneous samples, as already confirmed in our previous works [40,41]. These results illustrate that the  $\text{Sb}_2\text{Se}_3$ - $\text{In}_2\text{Se}_3$  ( $\beta$ ) composites were successfully synthesized without impurity phase.

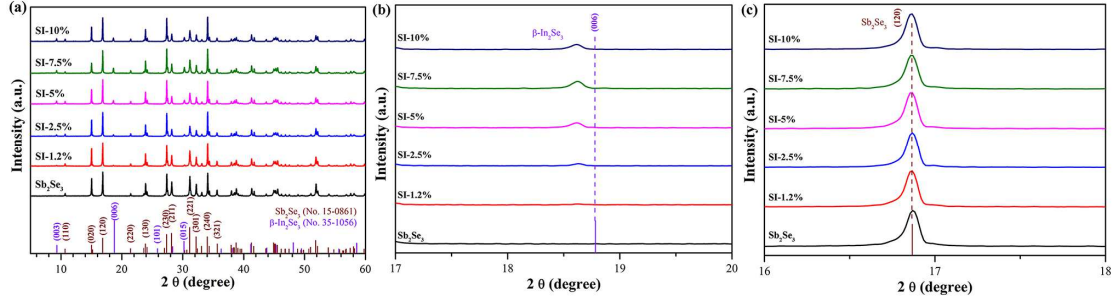


**Fig. 2.** (a) X-ray powder diffraction patterns for grinded samples prepared by in-situ melt-quenching method with different  $\beta$ - $\text{In}_2\text{Se}_3$  contents. (b) The enlarged (006) peak of  $\beta$ - $\text{In}_2\text{Se}_3$  and (c) (120) XRD peak of  $\text{Sb}_2\text{Se}_3$ .

### 3.2. Optical characterization and conductivity

Fig. 3a shows the direct band gap calculations based on the absorption spectra that were converted from diffuse reflectance data by using the Kubelka-Munk function [42].

The equation  $(F(R_\infty) \cdot hv)^{1/\gamma} = B(hv - E_g)$  can be obtained by combining the Kubelka-Munk and Tauc functions [42-45], where  $F(R_\infty)$  is proportional to the absorption coefficient ( $\alpha$ ),  $h$  is the Planck constant,  $\nu$  is the frequency,  $B$  is a constant related to effective mass, and  $E_g$  is the optical band gap of sample.  $\gamma$  has different values for direct band-gap (0.5) and indirect band-gap (2) semiconductor materials [46]. It can be seen that the value of direct band gap for pure  $\text{Sb}_2\text{Se}_3$  is 1.15 eV in agreement with earlier report [5]. For all the composites, the direct band gap values are found to be in the range of 1.15-1.18 eV, suggesting the composites have strong absorption of visible light. Except for SI-7.5% sample, the electrical conductivities of other samples increase with increasing  $\beta$ - $\text{In}_2\text{Se}_3$  molar fraction (Fig. 3b). According to the early report [31], the Sb-doped  $\beta$ - $\text{In}_2\text{Se}_3$  ( $\text{In}_{1.94}\text{Sb}_{0.06}\text{Se}_3$ ) has a good conductivity of  $2 \times 10^{-2} \text{ S} \cdot \text{cm}^{-1}$ , compared to the very low conductivity of pure  $\text{Sb}_2\text{Se}_3$ . Therefore, the improved conductivity of

the composites is likely due to the presence of the Sb-doped  $\beta$ - $\text{In}_2\text{Se}_3$  phase, as doped  $\text{Sb}_2\text{Se}_3$  was not observed on the XRD patterns. In brief, the composites have much better conductivity in comparison to the pure  $\text{Sb}_2\text{Se}_3$ , which could greatly enhance the transport of photogenerated charge carriers.

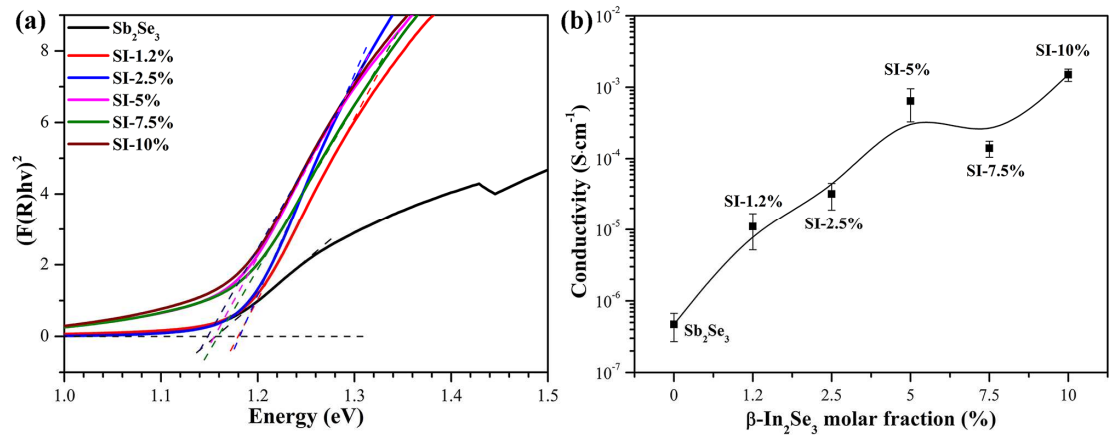


**Fig. 3.** (a) Tauc plots of the pure  $\text{Sb}_2\text{Se}_3$  and the  $\text{Sb}_2\text{Se}_3$ - $\text{In}_2\text{Se}_3$  ( $\beta$ ) composite powders with different  $\beta$ - $\text{In}_2\text{Se}_3$  contents. (b) The  $\beta$ - $\text{In}_2\text{Se}_3$  molar fraction dependence of conductivity at ambient temperature. The line is only for eye guidance.

### 3.3. Structure characterization and photoelectric performance

In order to verify the existence of heterojunctions inside the composites, the typical room temperature current-voltage (I-V) curves of all composites were measured with a wide range of voltage from -0.7 to 0.7 V. Two gold contacts were sputtered on the top and bottom surfaces of samples. The ohmic character of the gold contacts has been checked beforehand. It is clear from Fig. 4, in general, a non-ohmic characteristic indicates that the composites include heterojunctions, formed by more or less doped  $\text{Sb}_2\text{Se}_3/\beta$ - $\text{In}_2\text{Se}_3$ .

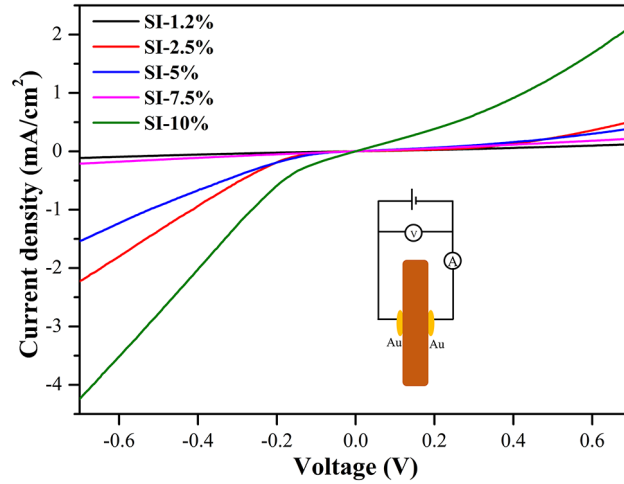


**Fig. 4.** I-V curves of the all composites showing a non-linear behavior, revealing the existence of heterojunctions.

The microstructural characterization of the composites was further used to investigate the influence of  $\text{Sb}_2\text{Se}_3/\beta\text{-In}_2\text{Se}_3$  heterojunction on the PEC performance measured by using the conventional three-electrode configuration (Fig. 5). Clearly, all composites show that the  $\beta\text{-In}_2\text{Se}_3$  has an acicular one-dimensional morphology. The values of photocurrent density for all samples were obtained at a bias voltage of  $-1.5\text{ V}$  vs.  $\text{Ag}/\text{AgCl}$  and under an illumination of  $7\text{ mW}/\text{cm}^2$ . As shown in Fig. 5a, the pure  $\text{Sb}_2\text{Se}_3$  shows a very weak photocurrent density of  $0.85\text{ }\mu\text{A}/\text{cm}^2$  in agreement with our previous work [15]. This can be attributed to the high recombination rate of photo-generated carriers due to the absence of heterojunction and to the difficulty of charge transport, associated with the low conductivity ( $4.7 \times 10^{-7}\text{ S}\cdot\text{cm}^{-1}$ ). After the formation of  $\beta\text{-In}_2\text{Se}_3$  in  $\text{Sb}_2\text{Se}_3$ , the photocurrent density was substantially enhanced due to the formation of  $\text{Sb}_2\text{Se}_3/\beta\text{-In}_2\text{Se}_3$  heterojunctions. Interestingly, the value of photocurrent density does not depend on the  $\beta\text{-In}_2\text{Se}_3$  molar fraction, but is related to the number of heterojunctions and the connectivity of  $\beta\text{-In}_2\text{Se}_3$ . It can be seen that a small number of

isolated  $\beta$ - $\text{In}_2\text{Se}_3$  crystals were formed in SI-1.2% sample (Fig. 5b). The photocurrent density of SI-1.2% sample was  $5.05 \mu\text{A}/\text{cm}^2$ , 6 times of that for pure  $\text{Sb}_2\text{Se}_3$ . This was attributed to the formation of  $\text{Sb}_2\text{Se}_3/\beta\text{-In}_2\text{Se}_3$  heterojunction and the improved electrical conductivity ( $1.1 \times 10^{-5} \text{ S}\cdot\text{cm}^{-1}$ ), which promoted the separation and transfer of photogenerated carriers. With increasing  $\beta\text{-In}_2\text{Se}_3$  contents, the bulk  $\text{Sb}_2\text{Se}_3$  was more and more intercalated with  $\beta\text{-In}_2\text{Se}_3$  crystals (Fig. 5c and d). The photocurrent density was greatly increased because of the formation of many  $\text{Sb}_2\text{Se}_3/\beta\text{-In}_2\text{Se}_3$  heterojunctions that made the separation of photoinduced electron-hole pairs more efficient. Moreover, the enhanced conductivity significantly facilitates the charge transport. Eventually, for SI-2.5% and SI-5% samples, the photocurrent density was 141.2 and  $121.7 \mu\text{A}/\text{cm}^2$ , about 166 and 143 times greater than that of pure  $\text{Sb}_2\text{Se}_3$ , respectively. Compared with SI-2.5% sample, the slightly declined photocurrent density of SI-5% sample was due to the increased size of  $\beta\text{-In}_2\text{Se}_3$  crystals. For the SI-7.5% sample (Fig. 5e), the size of  $\beta\text{-In}_2\text{Se}_3$  crystals was much larger as compared to those composites with lower  $\beta\text{-In}_2\text{Se}_3$  molar fraction (less than 7.5%), leading to reduced quantity of heterojunctions. Therefore, in despite of the improved conductivity ( $1.4 \times 10^{-4} \text{ S}\cdot\text{cm}^{-1}$ ), the photocurrent density was only  $15 \mu\text{A}/\text{cm}^2$ , much less than that of SI-2.5% sample. Surprisingly, plenty of connected and small  $\beta\text{-In}_2\text{Se}_3$  crystals were generated in SI-10% sample (Fig. 5f), accompanied by much higher conductivity of  $1.5 \times 10^{-3} \text{ S}\cdot\text{cm}^{-1}$  compared with SI-7.5% sample. This structure not only could effectively separate photogenerated electron-hole pairs but also fastly transferred them, due to the existence of abundant heterojunctions and connected  $\beta\text{-In}_2\text{Se}_3$  phase. As a result, the

photocurrent density was  $240.9 \mu\text{A}/\text{cm}^2$  for SI-10% sample. These results indicated that the number of heterojunctions and the connectivity of  $\beta\text{-In}_2\text{Se}_3$  crystals played an important role in the PEC performances of the composites.

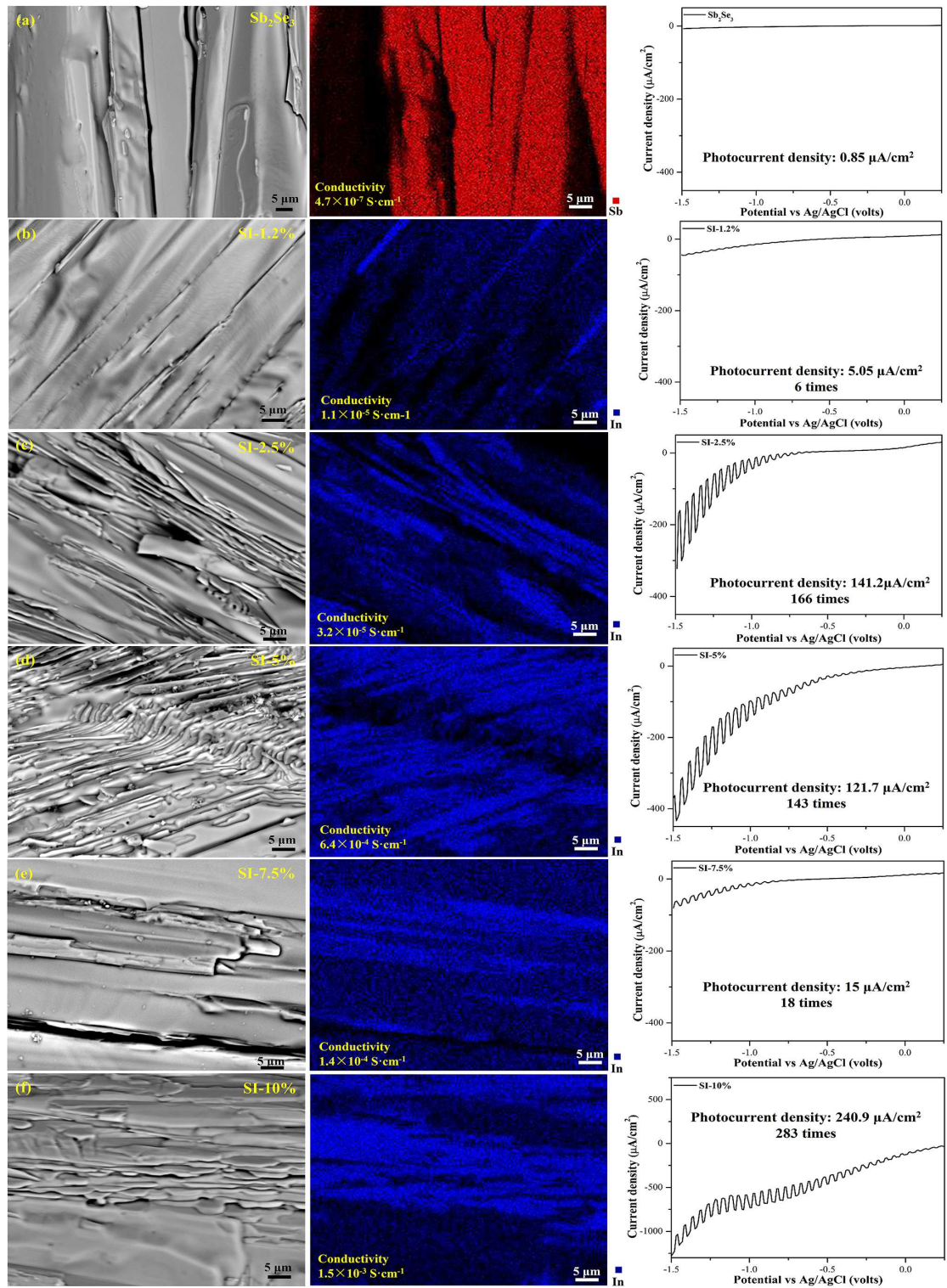


**Fig. 5.** Structure-dependent photocurrent density of the samples with elemental mapping of Sb or In. (a) Pure  $Sb_2Se_3$ ; (b) SI-1.2%; (c) SI-2.5%; (d) SI-5%; (e) SI-7.5%; (f) SI-10%.

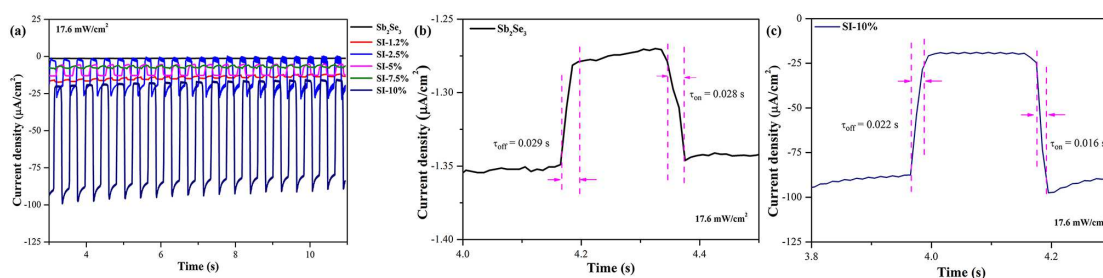
To further investigate the influence of  $Sb_2Se_3/\beta\text{-In}_2Se_3$  heterojunction on the

photo-response performances of the composites, the current density  $J$  - time  $T$  curves were characterized under an illumination of  $17.6 \text{ mW/cm}^2$  with a fixed bias of  $-0.7 \text{ V}$ . All composites exhibited an enhanced, stable and repeatable photocurrent response during several on-off cycles even in the electrolyte (Fig. 6a), revealing the excellent stability of the composites.

To evaluate the response time, magnified plots of one response cycle of pure  $\text{Sb}_2\text{Se}_3$  and SI-10% sample were shown in Fig. 6b and c. The photocurrent density of the pure  $\text{Sb}_2\text{Se}_3$  quickly increased from  $-1.27 \text{ }\mu\text{A/cm}^2$  (dark) to  $-1.35 \text{ }\mu\text{A/cm}^2$  (light) as the light was turned on. In contrast to pure  $\text{Sb}_2\text{Se}_3$ , the SI-10% sample shows a much more important photocurrent increase from  $-18.4 \text{ }\mu\text{A/cm}^2$  (dark) to  $-91.45 \text{ }\mu\text{A/cm}^2$  (light) due to the existence of internal heterojunctions. The response ( $\tau_{\text{on}}$ ) and recovery ( $\tau_{\text{off}}$ ) times were used to evaluate the response speed of the photocurrent during ON/OFF switching processes. The  $\tau_{\text{on}}$  represents the time spent for the photocurrent to increase from 10 to 90% values of the maximum current and the  $\tau_{\text{off}}$  displays the time required for the photocurrent to decrease from 90 to 10% values of the maximum current. The  $\tau_{\text{on}}$  and  $\tau_{\text{off}}$  for pure  $\text{Sb}_2\text{Se}_3$  are 0.028 s and 0.029 s, respectively. For SI-10% sample, both two values display a significant decrease to 0.016 s ( $\tau_{\text{on}}$ ) and 0.022 s ( $\tau_{\text{off}}$ ), which is attributed to higher crystal quality, preferential orientation, surface area, grain size and much more surface dangling bonds [13,47,48]. Meanwhile, the major factor causing the difference in response/recovery time may result from the traps and other defects, leading to the recombination of photo-generated carriers [49]. The sharp spike/dip of photocurrent during the on/off cycles for SI-10% sample indicates the fast

separation and transport of photoinduced carriers in this composite. It is worth noting that the response and recovery times are faster than that of previous reported  $\text{Sb}_2\text{Se}_3$  photodetectors [49,50], which suggests the  $\text{Sb}_2\text{Se}_3/\beta\text{-In}_2\text{Se}_3$  composites may have high application potential as excellent photodetectors.

Furthermore, the photosensitivity ( $S_{\text{ph}}$ ) of  $\text{Sb}_2\text{Se}_3$  and SI-10% samples can be calculated by the following equation:  $S_{\text{ph}} = (J_{\text{ph}} - J_{\text{d}})/J_{\text{d}}$  [35], where  $J_{\text{ph}}$  and  $J_{\text{d}}$  correspond the photocurrent density and the dark current density, respectively. The  $S_{\text{ph}}$  of SI-10% sample (1.37) is much larger than that of  $\text{Sb}_2\text{Se}_3$  (0.049), corresponding to a more efficient charge generation and transport upon illumination.



**Fig. 6.** (a) On/off cycle transient photoresponse of samples under illumination of 17.6 mW/cm<sup>2</sup> at -0.7 V. (b,c) Magnified plot of one response cycle of pure  $\text{Sb}_2\text{Se}_3$  and SI-10% sample.

STEM (Scanning transmission electron microscopy) image and EDS elemental mappings were further characterized in order to evidence the microstructure of  $\text{Sb}_2\text{Se}_3/\beta\text{-In}_2\text{Se}_3$  composite (Fig. 7a). Clearly, it can be seen that the In element is mainly enriched in the bright region, corresponding to the  $\beta\text{-In}_2\text{Se}_3$ , whereas the color variation of Sb and Se elements is related to a thickness. The different thicknesses resulted in the underestimation of Se element, which was often observed in measurements of interface composition by STEM-EDS [51]. In fact, this thickness variation witnesses a higher

resistance of  $\beta$ - $\text{In}_2\text{Se}_3$  towards the ion beam used for TEM sample preparation (ionic thinning of the sample). Fig. 7b shows the EDS line scanning result of the black line marked in Fig. 7a. It reveals that the  $\beta$ - $\text{In}_2\text{Se}_3$  is doped with Sb, in agreement with the result obtained from XRD patterns (Fig. 2). At the same time, the atomic ratio of In/Sb/Se is close to 1:1:3 in Sb-doped  $\beta$ - $\text{In}_2\text{Se}_3$  ( $\text{InSbSe}_3$ ) and the dark region is  $\text{Sb}_2\text{Se}_3$ , which is confirmed by subsequent SAED patterns (Fig. 8). Based on the above results, it is confirmed that the composite is consisted of the intercalated Sb-doped  $\beta$ - $\text{In}_2\text{Se}_3$  and  $\text{Sb}_2\text{Se}_3$ , with strong interfacial chemical interaction.

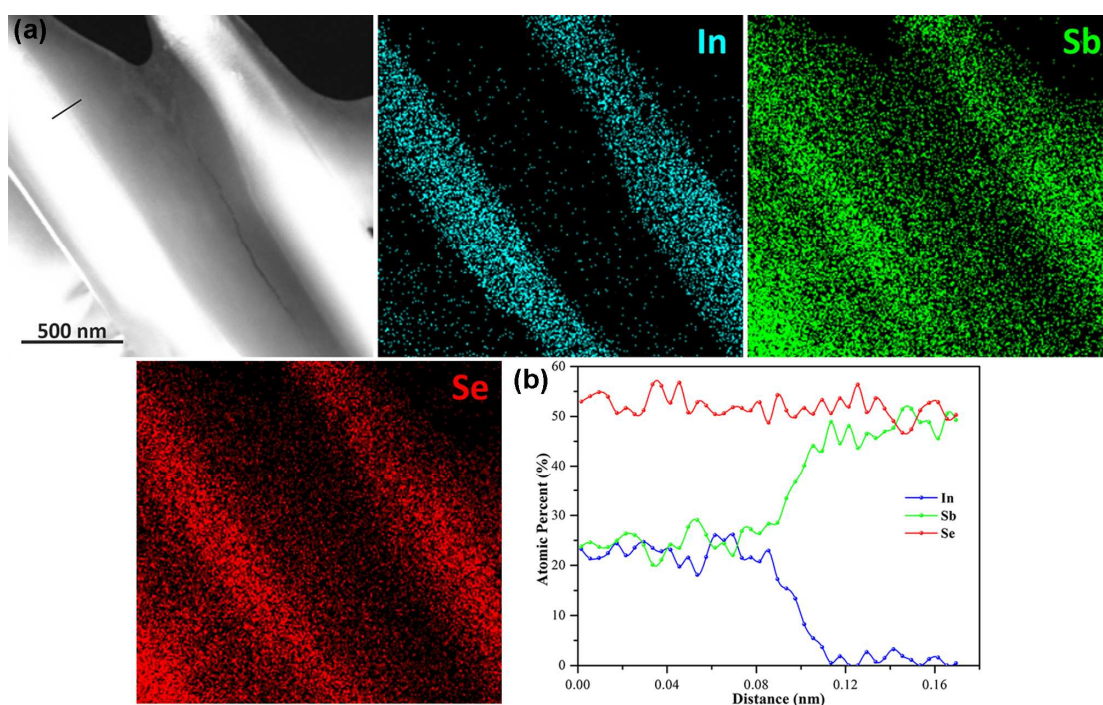


**Fig. 7.** (a) STEM image and EDS elemental mappings of  $\text{Sb}_2\text{Se}_3/\beta\text{-In}_2\text{Se}_3$  heterojunction composite. (b) EDS line scanning result of the interface of  $\text{Sb}_2\text{Se}_3/\beta\text{-In}_2\text{Se}_3$  obtained from black line marked in (a). Color variation of Sb and Se is related to the thickness fluctuation of the sample.

Fig. 8 shows the TEM, SAED and HRTEM images of the  $\text{Sb}_2\text{Se}_3/\beta\text{-In}_2\text{Se}_3$  heterojunction composite, indicating the formation of  $\text{Sb}_2\text{Se}_3/\beta\text{-In}_2\text{Se}_3$  ( $\text{InSbSe}_3$ )

heterojunction composite, in agreement with the results of XRD. In addition, the planes (020) of  $\text{Sb}_2\text{Se}_3$  and (110) of  $\text{InSbSe}_3$  (Sb-doped  $\beta\text{-In}_2\text{Se}_3$ ) are oriented in the same direction by following the boundary between the two phases. Fig. 8c presents the HRTEM image of composite, showing clearly the heterojunction interface between  $\text{Sb}_2\text{Se}_3$  and  $\text{InSbSe}_3$  (Sb-doped  $\beta\text{-In}_2\text{Se}_3$ ).

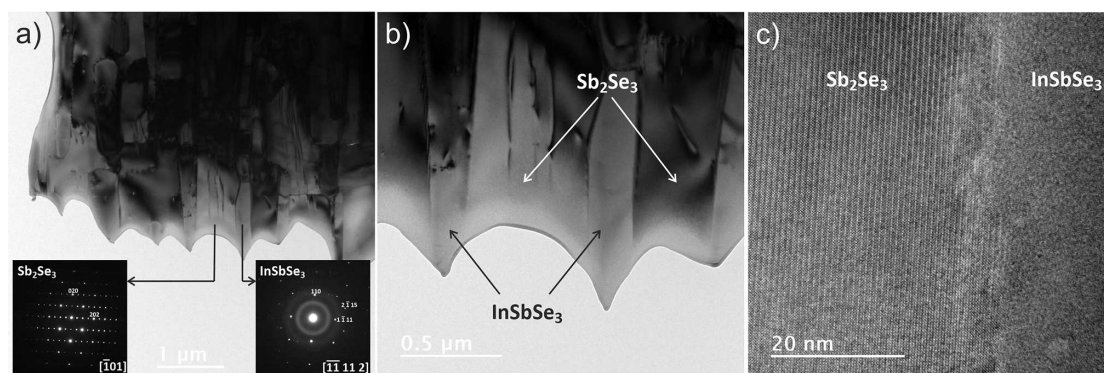


**Fig. 8.** (a,b) TEM bright field images and SAED patterns of  $\text{Sb}_2\text{Se}_3/\beta\text{-In}_2\text{Se}_3$  heterojunction composite. (c) HRTEM image showing the interface between  $\text{Sb}_2\text{Se}_3$  and  $\text{InSbSe}_3$  (Sb-doped  $\beta\text{-In}_2\text{Se}_3$ ).

### 3.4. Mechanism of enhanced photoelectric performance

Although the  $\text{Sb}_2\text{Se}_3/\beta\text{-In}_2\text{Se}_3$  heterojunction significantly facilitated the separation and transfer of photogenerated electron-hole pairs, it is interesting to fully understand the mechanism. In order to draw the band diagram, the values of the conduction band minimum (CBM), valence band maximum (VBM), Fermi level and band gap energy were adopted from published data [22, 52]. The CBM, VBM, Fermi level and band gap of  $\beta\text{-In}_2\text{Se}_3$  are respectively -4.44, -5.79, -4.51 and 1.35 eV. For  $\text{Sb}_2\text{Se}_3$ , these values are -4.15, -5.35, -4.75 and 1.2 eV, respectively. According to the band gap structure of  $\text{Sb}_2\text{Se}_3$  and  $\beta\text{-In}_2\text{Se}_3$ , the separation and transportation processes of photoinduced electrons and holes can be described in Fig. 9. The  $\text{Sb}_2\text{Se}_3/\beta\text{-In}_2\text{Se}_3$

heterojunction is formed after contact, with a type-II band alignment. The built-in electric field is directed from n-type  $\beta$ - $\text{In}_2\text{Se}_3$  to p-type  $\text{Sb}_2\text{Se}_3$ . Upon illumination, the  $\text{Sb}_2\text{Se}_3$  and  $\beta$ - $\text{In}_2\text{Se}_3$  both absorb incident light due to their narrow direct band gaps, photogenerated electrons can be excited from the VB into CB (solid green arrows), and electrons easily flow from the CB of  $\text{Sb}_2\text{Se}_3$  to the CB of  $\beta$ - $\text{In}_2\text{Se}_3$  (green dotted arrow). Meanwhile, the holes can transfer from the VB of  $\beta$ - $\text{In}_2\text{Se}_3$  to the VB of  $\text{Sb}_2\text{Se}_3$  (red dotted arrow). In this bandgap model, the photoinduced electron-hole pairs can be readily separated and transferred, minimizing their recombination, and thus the photocurrent density and the ON/OFF response speed of composites with  $\text{Sb}_2\text{Se}_3/\beta$ - $\text{In}_2\text{Se}_3$  p-n heterojunctions are significantly enhanced.

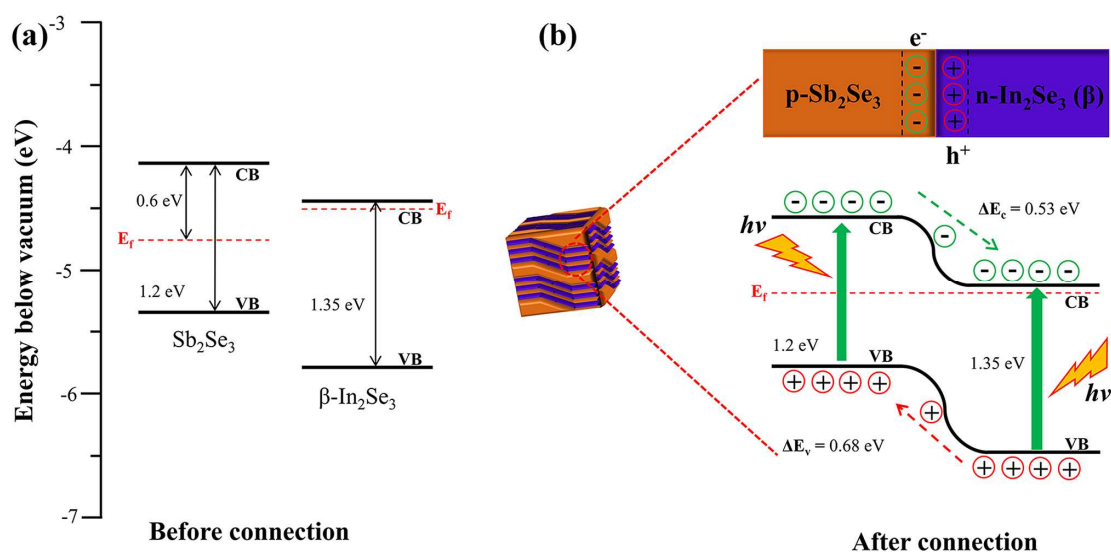


**Fig. 9.** Schematic illustration of photoinduced electron-hole separation and transfer in  $\text{Sb}_2\text{Se}_3/\beta$ - $\text{In}_2\text{Se}_3$  heterojunction.

### 3.5. Photocatalytic activity of SI-10% sample for MO dye decomposition

In general, sulfide/selenide photocatalysts can have excellent photocatalytic performance [53-56]. Considering the remarkable photocurrent density and the

excellent stability of the SI-10% sample, it was tested for photodegradation of MO dye. As discussed before,  $\beta$ - $\text{In}_2\text{Se}_3$  is metastable at normal pressure and temperature and is therefore difficult to obtain at room temperature [30]. As a result, the photocatalytic activities of the SI-10% sample was compared to pure  $\text{Sb}_2\text{Se}_3$  and the results are shown in Fig. 10. Clearly, the characteristic absorption peak of MO is located at 464 nm, and it is rapidly weakened with time, indicating the decomposition of the MO molecular structure. The decomposition of MO solution as a function of illumination time is presented in Fig. 10c, where C is the MO concentration after light illumination, and  $C_0$  is the initial MO concentration after reaching the adsorption-desorption equilibrium in the dark. As a comparison, the photolytic activity of the catalyst-free MO solution (Blank) is almost negligible, evidencing the photochemical stability of MO molecule. The photocatalyst can form major reactive species ( $\text{O}_2^{\cdot-}$  and  $\text{OH}^{\cdot}$ ) via the reaction between photogenerated electron-hole pairs and adsorbed surface substance ( $\text{O}_2$  and  $\text{OH}^-$ ) under light illumination, which can spontaneously degrade pollutant organic molecules (MO), as already evidenced by other authors [57,58]. Consequently, the MO concentration declines with prolonged illumination time. After 180 min of illumination, 76% and 90% of MO dye has been decomposed with SI-10% sample and pure  $\text{Sb}_2\text{Se}_3$ , respectively, in spite of the much lower specific surface area of the SI-10% sample, as shown in Table 1. Furthermore, the  $\text{Sb}_2\text{Se}_3/\beta\text{-In}_2\text{Se}_3$  composite was stable after the photocatalytic reactions, indicated by the XRD patterns in Fig. 10d.

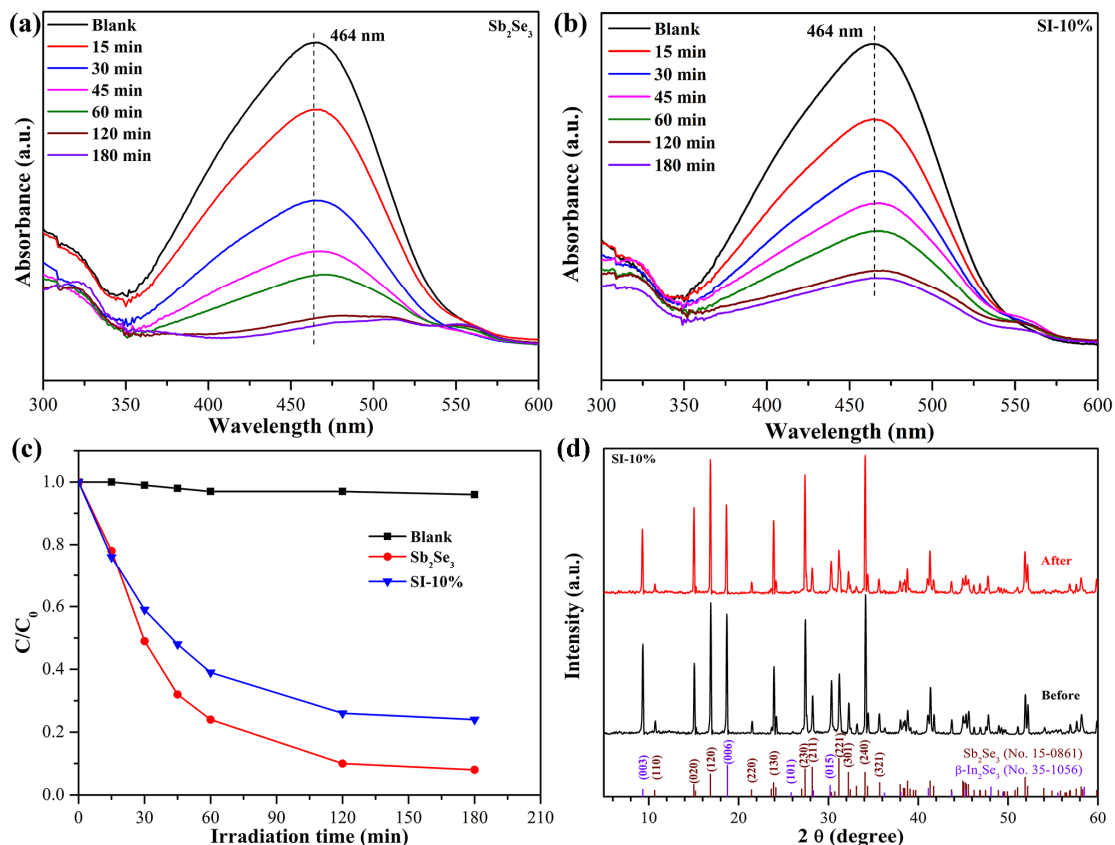


**Fig. 10.** The UV-vis absorption spectra of MO solutions before and after the photocatalytic decomposition with (a)  $Sb_2Se_3$  and (b) SI-10% sample as photocatalyst, respectively. (c) Degradation profiles of MO solution under white light illumination. (d) The XRD patterns of SI-10% sample before and after the photocatalytic reactions.

**Table 1** The BET surface areas of pure  $Sb_2Se_3$  and SI-10% sample.

Samples	$Sb_2Se_3$	SI-10%
BET area ( $m^2 \cdot g^{-1}$ )	2.4	1.5

## 4. Conclusions

In summary, a series of  $Sb_2Se_3/\beta-In_2Se_3$  heterojunction composites with different contents of  $\beta-In_2Se_3$  have been successfully synthesized via an in-situ

melt-quenching method. The direct band gap energy of the composites was in the range of 1.15-1.18 eV, **ensuring an efficient harvesting of visible light**. Compared with pure  $\text{Sb}_2\text{Se}_3$ , the  $\text{Sb}_2\text{Se}_3/\beta\text{-In}_2\text{Se}_3$  composites displayed remarkable photoelectric performances and excellent stability even in 0.5 M  $\text{LiClO}_4$  aqueous electrolyte. The highest photocurrent density was obtained with the composite ( $\text{Sb}_2\text{Se}_3$ -10%  $\beta\text{-In}_2\text{Se}_3$ ) consisted of abundant heterojunctions and highly connected  $\beta\text{-In}_2\text{Se}_3$  crystals, and was 283 times higher than that of pure  $\text{Sb}_2\text{Se}_3$ . Meanwhile, the response and recovery times of the composite were significantly faster than that of pure  $\text{Sb}_2\text{Se}_3$ . The enhanced photoelectric performances were attributed to the heterojunction between  $\text{Sb}_2\text{Se}_3$  and doped  $\beta\text{-In}_2\text{Se}_3$ , which facilitated the separation and transport of photogenerated charge carriers. More importantly, the composite possesses interesting photocatalytic activity, illustrated by photocatalytic MO degradation. After 180 min of illumination, 76% of MO dye could be decomposed. We believe this work would provide direct guidance for constructing efficient  $\text{Sb}_2\text{Se}_3/\beta\text{-In}_2\text{Se}_3$  heterojunction devices for different applications such as photo-catalysis, solar cell and photodetector.

## **Conflicts of interest**

There are no conflicts to declare.

## **Acknowledgements**

We gratefully acknowledge the China Scholarship Council for providing financial

support (201804910786) for D.R. to stay at the ISCR. We thank Nathalie Herbert for the measurement of nitrogen adsorption isotherms. We would like to acknowledge the assistance on XRD data received from François Cheviré and Franck Tessier. We also thank Antoine Vacher for his contribution in the band gap characterization.

## References

- [1] J. Ren, W. Que, X. Yin, Y. He, H.M.A. Javed, Novel fabrication of TiO<sub>2</sub>/ZnO nanotube array heterojunction for dye-sensitized solar cells, *RSC Adv.* 4 (2014) 7454-7460.
- [2] Y. Liu, X. Sun, B. Li, Y. Lei, Tunable p-n transition behaviour of a p-La<sub>0.67</sub>Sr<sub>0.33</sub>MnO<sub>3</sub>/n-CeO<sub>2</sub> nanofibers heterojunction for the development of selective high temperature propane sensors, *J. Mater. Chem. A* 2 (2014) 11651-11659.
- [3] M. Faisal, F. Harraz, A. Ismail, A. El-Toni, S. AlSayari, A. AlHajry, M. AlAssiri, Novel mesoporous NiO/TiO<sub>2</sub> nanocomposites with enhanced photocatalytic activity under visible light illumination, *Ceram. Int.* 44 (2018) 7047-7056.
- [4] C. Chen, Y. Yang, D.C. Bobela, S. Lu, K. Zeng, B. Yang, L. Gao, M.C. Beard, J. Tang, Characterization of basic physical properties of Sb<sub>2</sub>Se<sub>3</sub> and its relevance for photovoltaics, *Front. Optoelectron.* 10 (2017) 18-30.
- [5] C. Chen, W. Li, Y. Zhou, C. Chen, M. Luo, X. Liu, K. Zeng, B. Yang, C. Zhang, J. Han, J. Tang, Optical properties of amorphous and polycrystalline Sb<sub>2</sub>Se<sub>3</sub> thin films prepared by thermal evaporation, *Appl. Phys. Lett.* 107 (2015) 043905.
- [6] D. Choi, Y. Jang, J. Lee, G.H. Jeong, D. Whang, S.W. Hwang, K.S. Cho, S.W. Kim, Diameter-controlled and surface-modified Sb<sub>2</sub>Se<sub>3</sub> nanowires and their photodetector performance, *Sci. Rep.* 4 (2015) 6714.
- [7] Z. Li, X. Chen, H. Zhu, J. Chen, Y. Guo, C. Zhang, W. Zhang, X. Niu, Y. Mai, Sb<sub>2</sub>Se<sub>3</sub> thin film solar cells in substrate configuration and the back contact selenization, *Sol. Energy Mater. Sol. Cells* 161 (2017) 190-196.
- [8] H. Guo, Z. Chen, X. Wang, Q. Cang, C. Ma, X. Jia, N. Yuan, J. Ding, Significant increase in efficiency and limited toxicity of a solar cell based on Sb<sub>2</sub>Se<sub>3</sub> with SnO<sub>2</sub> as a buffer layer, *J. Mater. Chem. C* 7 (2019) 14350-14356.
- [9] D. Ren, S. Chen, M. Cathelinaud, G.-X. Liang, H. Ma, X. Zhang, Fundamental physical characterization of Sb<sub>2</sub>Se<sub>3</sub>-based quasi-homojunction thin film solar cells, *ACS Appl. Mater. Interfaces* DOI: 10.1021/acsami.0c08180.
- [10] R.R. Prabhakar, W. Septina, S. Siol, T. Moehl, R. Wick-Joliat, S.D. Tilley, Photocorrosion-resistant Sb<sub>2</sub>Se<sub>3</sub> photocathodes with earth abundant MoS<sub>x</sub> hydrogen evolution catalyst, *J. Mater. Chem. A* 5 (2017) 23139-23145.
- [11] D. An, S. Chen, Z. Lu, R. Li, W. Chen, W. Fan, W. Wang, Y. Wu, Low thermal conductivity and optimized thermoelectric properties of p-type Te-Sb<sub>2</sub>Se<sub>3</sub>: synergistic effect of doping and defect engineering, *ACS Appl. Mater. Interfaces* 11 (2019) 27788-27797.
- [12] B.R. Chakraborty, B. Ray, R. Bhattacharya, A.K. Dutta, Magnetic and electric properties of antimony selenide (Sb<sub>2</sub>Se<sub>3</sub>) crystals, *J. Phys. Chem. Solids* 41 (1980) 913-917.
- [13] S. Chen, X. Qiao, Z. Zheng, M. Cathelinaud, H. Ma, X. Fan, X. Zhang, Enhanced electrical conductivity and photoconductive properties of Sn-doped Sb<sub>2</sub>Se<sub>3</sub> crystals, *J. Mater. Chem. C* 6 (2018) 6465-6470.
- [14] W. Wu, Y. Li, L. Liang, Q. Hao, J. Zhang, H. Liu, C. Liu, Enhanced broadband responsivity of Ni-doped Sb<sub>2</sub>Se<sub>3</sub> nanorod photodetector, *Phys. Chem. C* 123 (2019) 14781-14789.
- [15] X. Zhang, Y. Xu, Q. Shen, B. Fan, X. Qiao, X. Fan, H. Yang, Q. Luo, L. Calvez, H. Ma, M. Cathelinaud, J.J. Simon, Enhancement of charge photo-generation and transport via an internal network of Sb<sub>2</sub>Se<sub>3</sub>/Cu<sub>2</sub>GeSe<sub>3</sub> heterojunctions, *J. Mater. Chem. A* 2 (2014) 17099-17106.

- [16] S.P. Anthony, Synthesis of Ag<sub>2</sub>S and Ag<sub>2</sub>Se nanoparticles in self assembled block copolymer micelles and nano-arrays fabrication, *Mater. Lett.* 63 (2009) 773-776.
- [17] J. Ye, S. Soeda, Y. Nakamura, O. Nittimo, Crystal structures and phase transformation in In<sub>2</sub>Se<sub>3</sub> compound semiconductor, *Jpn. J. Appl. Phys.* 37 (1998) 4264-4271.
- [18] P. Patel, V. Patel, S. Vyas, J. Patel, H. Pavagadhi, Optical investigations of In<sub>2</sub>Se<sub>2.7</sub>Sb<sub>0.3</sub> thin films prepared by thermal evaporation technique, *Mater. Sci. Forum* 969 (2019) 355-360.
- [19] H. Bouzouita, N. Bouguila, S. Duchemin, S. Fiechter, A. Dhouib, Preparation and characterization of In<sub>2</sub>Se<sub>3</sub> thin films, *Renewable Energy* 25 (2002) 131-138.
- [20] X.F. Wei, L.W. Li, H.G. Feng, J.B. Gong, K. Jiang, S.L. Xue, Preparation and optical properties of In<sub>2</sub>Se<sub>3</sub> nanospheres using CTAB as surface modifier, *Ceram. Int.* 46 (2020) 1026-1032.
- [21] T. Li, J. Wang, J. Lai, X. Zheng, W. Liu, J. Ji, H. Liu, Z. Jin, Multi-morphological growth of nano-structured In<sub>2</sub>Se<sub>3</sub> by ambient pressure triethylene glycol based solution syntheses, *J. Alloys Compd.* 646 (2015) 603-611.
- [22] Z. Zheng, J. Yao, G. Yang, Self-assembly of the lateral In<sub>2</sub>Se<sub>3</sub>/CuInSe<sub>2</sub> heterojunction for enhanced photodetection, *ACS Appl. Mater. Interfaces* 9 (2017) 7288-7296.
- [23] J. Igo, S. Zhou, Z.G. Yu, O.P. Amnuayphol, F. Zhao, Y. Gu, Anharmonic phonon coupling in single-crystal semiconducting and metal-like van der Waals In<sub>2</sub>Se<sub>3</sub>, *J. Phys. Chem. C* 122 (2018) 22849-22855.
- [24] X. Li, X. Zuo, H. Li, L. Han, Q. Gao, D. Li, B. Cui, D. Liu, F. Qu, Exotic magnetism in As-doped  $\alpha/\beta$ -In<sub>2</sub>Se<sub>3</sub> monolayers with tunable anisotropic carrier mobility, *Phys. Chem. Chem. Phys.* 21 (2019) 19234-19241.
- [25] J. Jasinski, W. Swider, J. Washburn, Z. Liliental-Weber, A. Chaiken, K. Nauka, G.A. Gibson, C.C. Yang, Crystal structure of  $\kappa$ -In<sub>2</sub>Se<sub>3</sub>, *Appl. Phys. Lett.* 81 (2002) 4356-4358.
- [26] B. Thomas, Effect of in situ post-deposition annealing on the formation of  $\alpha$ -In<sub>2</sub>Se<sub>3</sub> thin films grown by elemental evaporation, *Appl. Phys. A: Mater. Sci. Process.* 54 (1992) 293-299.
- [27] C. Julien, A. Chevy, D. Siapkias, Optical properties of In<sub>2</sub>Se<sub>3</sub> phases, *Phys. Status Solidi A* 118 (1990) 553-559.
- [28] G. Han, Z.G. Chen, J. Drennan, J. Zou, Indium selenides: structural characteristics, synthesis and their thermoelectric performances, *Small* 10 (2014) 2747-2765.
- [29] S. Popovic, A. Tonejc, B. Grzeta-Plenkovic, B. Celustka, R. Trojko, Revised and new crystal data for indium selenides, *J. Appl. Crystallogr.* 12 (1979) 416-420.
- [30] C. Amory, J.C. Bernede, S. Marsillac, Study of a growth instability of  $\gamma$ -In<sub>2</sub>Se, *J. Appl. Phys.* 94 (2003) 6945-6948.
- [31] D. Eddike, A. Ramdani, G. Brun, J.C. Tedenac, B. Liautard, Phase diagram equilibria In<sub>2</sub>Se<sub>3</sub>-Sb<sub>2</sub>Se<sub>3</sub> crystal growth of the  $\beta$ -In<sub>2</sub>Se<sub>3</sub> phase (In<sub>1.94</sub>Sb<sub>0.06</sub>Se<sub>3</sub>), *Mater. Res. Bull.* 33 (1998) 519-523.
- [32] D. Ren, Z. Zheng, M. Wei, P. Zhang, M. Cathelinaud, H. Ma, X. Zhang, Synthesis, structure and photoelectric properties of selenide composites with in situ constructed Sb<sub>2</sub>Se<sub>3</sub>/NaSbSe<sub>2</sub> heterojunction, *J. Eur. Ceram. Soc.* 40 (2020) 4517-4526.
- [33] H. Peng, X. Zhang, R.D. Twisten, Y. Cui, Vacancy ordering and lithium insertion in III<sub>2</sub>VI<sub>3</sub> nanowires, *Nano Res.* 2 (2009) 327-335.
- [34] D.T. Schoen, H. Peng, Y. Cui, Anisotropy of chemical transformation from In<sub>2</sub>Se<sub>3</sub> to CuInSe<sub>2</sub> nanowires through solid state reaction, *J. Am. Chem. Soc.* 131 (2009) 7973-7975.
- [35] C.J. Diliegros-Godines, J.S. Cruz, N.R. Mathews, M. Pal, Effect of Ag doping on structural,

- optical and electrical properties of antimony sulfide thin films, *J. Mater. Sci.* 53 (2018) 11562-11573.
- [36] S. Bhatia, N. Verma, Gas sensing performance of dip-coated indium-doped ZnO films, *J. Electron. Mater.* 47 (2018) 6450-6457.
- [37] J. Cui, L. Wang, Z. Du, P. Ying, Y. Deng, High thermoelectric performance of a defect in  $\alpha$ -In<sub>2</sub>Se<sub>3</sub>-based solid solution upon substitution of Zn for In, *J. Mater. Chem. C* 3 (2015) 9069-9075.
- [38] Y. Min, G.D. Moon, J. Park, M. Park, U. Jeong, Surfactant-free CuInSe<sub>2</sub> nanocrystals transformed from In<sub>2</sub>Se<sub>3</sub> nanoparticles and their application for a flexible UV photodetector, *Nanotechnology* 22 (2011) 465604-465613.
- [39] H. Ji, A. Reijnders, T. Liang, L.M. Schoop, K.S. Burch, N.P. Ong, R.J. Cava, Crystal structure and elementary electronic properties of Bi-stabilized  $\alpha$ -In<sub>2</sub>Se<sub>3</sub>, *Mater. Res. Bull.* 48 (2013) 2517-2521.
- [40] D. Ren, Q. Deng, J. Wang, Y. Li, M. Li, S. Ran, S. Du, Q. Huang, Densification and mechanical properties of pulsed electric current sintered B<sub>4</sub>C with in situ synthesized Al<sub>3</sub>BC obtained by the molten-salt method, *J. Eur. Ceram. Soc.* 37 (2017) 4524-4531.
- [41] D. Ren, Q. Deng, J. Wang, J. Yang, Y. Li, J. Shao, M. Li, J. Zhou, S. Ran, S. Du, Q. Huang, Synthesis and properties of conductive B<sub>4</sub>C ceramic composites with TiB<sub>2</sub> grain network, *J. Am. Ceram. Soc.* 101 (2018) 3780-3786.
- [42] P. Makuła, M. Pacia, W. Macyk, How to correctly determine the band gap energy of modified semiconductor photocatalysts based on U-Vis spectra, *J. Phys. Chem. Lett.* 9 (2018) 6814-6817.
- [43] P. Kubelka, New contributions to the optics of intensely light-scattering materials. Part I, *J. Opt. Soc. Am.* 38 (1948) 448-457.
- [44] V. Džimbeg-malčić, Ž. Barbarić-mikočević, K. Itrić, Kubelka-munk theory in describing optical properties of paper (II), *Technol. Gaz.* 19 (2012) 191-196.
- [45] L. Yang, B. Kruse, Revised kubelka-munk theory. I. Theory and application, *J. Opt. Soc. Am. A* 21 (2004) 1933-1941.
- [46] J.I. Pankove, *Optical progresses in semiconductors*, 2<sup>nd</sup> edition, Dover, New York, 2010.
- [47] K. Zhang, T. Luo, H. Chen, Z. Lou, G. Shen, Au-nanoparticles-decorated Sb<sub>2</sub>S<sub>3</sub> nanowire-based flexible ultraviolet/visible photodetectors, *J. Mater. Chem. C* 5 (2017) 3330-3335.
- [48] W. Zhou, Y. Peng, Y. Yin, Y. Zhou, Y. Zhang, D. Tang, Broad spectral response photodetector based on individual tin-doped CdS nanowire, *AIP Adv.* 4 (2014) 123005.
- [49] Y.Q. Liu, M. Zhang, F.X. Wang, G.B. Pan, Facile microwave-assisted synthesis of uniform Sb<sub>2</sub>Se<sub>3</sub> nanowires for high performance photodetectors, *J. Mater. Chem. C* 2 (2014) 240-244.
- [50] T. Zhai, M. Ye, L. Li, X. Fang, M. Liao, Y. Li, Y. Koide, Y. Bando, D. Golberg, Single-crystalline Sb<sub>2</sub>Se<sub>3</sub> nanowires for high-performance field emitters and photodetectors, *Adv. Mater.* 22 (2010) 4530-4533.
- [51] S.R. Spurgeon, Y. Du, S.A. Chambers, Measurement error in atomic-scale STEM-EDS mapping of a model oxide interface, arXiv preprint arXiv: 1610.03432 (submitted to *Microsc. Microanal.*).
- [52] X. Liu, J. Chen, M. Luo, M. Leng, Z. Xia, Y. Zhou, S. Qin, D.J. Xue, L. Lv, H. Huang, D. Niu, J. Tang, Thermal evaporation and characterization of Sb<sub>2</sub>Se<sub>3</sub> thin film for substrate Sb<sub>2</sub>Se<sub>3</sub>/CdS solar cells, *ACS Appl. Mater. Interfaces* 6 (2014) 10687-10695.
- [53] X. Liu, Z. Xing, Y. Zhang, Z. Li, X. Wu, S. Tan, X. Yu, Q. Zhu, W. Zhou, Fabrication of 3D

- flower-like black N-TiO<sub>2-x</sub>@MoS<sub>2</sub> for unprecedented-high visible-light-driven photocatalytic performance, *Appl. Catal., B* 201 (2017) 119-127.
- [54] B. Sun, W. Zhou, H. Li, L. Ren, P. Qiao, W. Li, H. Fu, Synthesis of particulate hierarchical tandem heterojunctions toward optimized photocatalytic hydrogen production, *Adv. Mater.* 30 (2018) 1804282.
- [55] X. Liu, Z. Xing, H. Zhang, W. Wang, Y. Zhang, Z. Li, X. Wu, X. Yu, W. Zhou, Fabrication of 3D mesoporous black TiO<sub>2</sub>/MoS<sub>2</sub>/TiO<sub>2</sub> nanosheets for visible-light-driven photocatalysis, *ChemSusChem* 9 (2016) 1118-1124.
- [56] Y.B. Kim, S.W. Cho, N.G. Deshpande, S.H. Jung, D.S. Kim, K.J. Park, H.-K. Kim, H.K. Cho, Smart bifunctional Sb<sub>2</sub>Se<sub>3</sub> nanorods for integrated water purification: Insoluble liquid separation and photoelectrochemical degradation, *ChemSusChem* 13 (2020) 3017-3027.
- [57] H. Zhang, C. Hu, Y. Ding, Y. Lin, Synthesis of 1D Sb<sub>2</sub>S<sub>3</sub> nanostructures and its application in visible-light-driven photodegradation for MO, *J. Alloys Compd.* 625 (2015) 90-94.
- [58] R. Cai, J.-G. Wu, L. Sun, Y.-J. Liu, T. Fang, S. Zhu, S.-Y. Li, Y. Wang, L.-F. Guo, C.-E. Zhao, A. Wei, 3D graphene/ZnO composite with enhanced photocatalytic activity, *Mater. Des.* 90 (2016) 839-844.